Journal of Rock Mechanics and Geotechnical Engineering 18 (2026) 3606–3622

Contents lists available at ScienceDirect

Journal of Rock Mechanics and Geotechnical Engineering

journal homepage: www.jrmge.cn

Full Length Article

Borehole breakout in heterogeneous rocks using improved Voronoi model: Laboratory test and discrete element modeling

Yingchun Li [a,*], Jiazhi Zhang [a], Changyi Zuo [b,**], Kang Duan [c]

[a] Department of Civil Engineering, State Key Laboratory of Coastal and Offshore Engineering, Dalian University of Technology, Dalian, 116024, China
[b] School of Civil and Environmental Engineering, University of New South Wales, Sydney, NSW, 2052, Australia
[c] School of Civil Engineering, Shandong University, Jinan, 250100, China

ARTICLE INFO

Article history:
Received 25 February 2025
Received in revised form
25 June 2025
Accepted 29 June 2025
Available online 10 July 2025

Keywords:
Borehole breakout
Rock heterogeneity
Discrete element model (DEM)
Weibull distribution
Sandstone
Voronoi model

ABSTRACT

Borehole instability in heterogeneous rocks poses a significant challenge in geo-energy engineering. The deformation and failure around boreholes are heavily mediated by the inherent heterogeneity of rocks. Here, we examined borehole breakout under hydrostatic pressure through both laboratory tests and numerical simulations on sandstone samples. Laboratory experiments demonstrated symmetrical V-shaped failures across various borehole diameters. To replicate these observations, we developed a heterogenous UDEC Voronoi model where the material heterogeneity was interpreted by assigning Weibull-distributed inter-grain contact parameters. The rigorous-calibrated numerical modeling can effectively capture the microscopic damage process and match the observed macroscopic failure modes. Simulations showed that reducing the borehole diameter increases the critical hydrostatic pressure required for borehole failure and prompts a shift from tensile to shear-dominated failure behavior. While stress anisotropy primarily governs the overall breakout morphology, rock heterogeneity influences the specific locations of crack initiation, leading to localized stress concentrations that shape the ultimate failure patterns. These results provide valuable insights into borehole stability in heterogeneous rocks and guide engineering design and pertinent risk assessment.

1. Introduction

Borehole breakout, representing the localized failure and resulting geometric deformation of borehole cross-sections, poses severe challenges in wide geo-energy engineering (Haimson and Song, 1993). This phenomenon arises when drilling operations disturb the original stress state of rock masses—materials known for their discontinuous, heterogeneous, and anisotropic nature. The stress redistribution and concentration surrounding the borehole often can lead to excavation damage zones and potential instabilities, which can adversely affect the integrity of boreholes, tunnels, and shafts.

Systematic studies on borehole breakout trace back to observation of stress-induced spalling in South African gold mine shaft walls (Leeman, 1999). Advancements in the late 1970s and early 1980s, aided by four-arm calipers and borehole imaging techniques, unveiled excavation damage zones that consistently oriented toward the minimum horizontal principal stress (Bell and Gough, 1979; Gough and Bell, 1981; Plumb and Hickman, 1985; Zoback et al., 1985). This correlation was soon corroborated by laboratory testing, which further demonstrated how in situ stress conditions govern the dimensions of failure zones (Haimson and Song, 1993). Extensive laboratory studies on various rock types have revealed three main failure modes—V-shaped (dog ear), spiral, and groove—each linked to distinct fracture mechanisms (Fig. 1) (Addis et al., 1990; Ewy and Cook, 1990; Herrick and Haimson, 1994; Van Den Hoek, 2001; Cuss et al., 2003; Haimson and Kovacich, 2003; Haimson and Lee, 2004; Cerasi et al., 2005; Haimson, 2007; Papamichos, 2010; Meier et al., 2013; Lee et al., 2016). V-shaped failure can stem from either shear rupture or tensile spalling, or a combination of both. Under shear-dominated conditions, fractures propagate from the borehole wall as shear zones, whereas tensile spalling typically initiates cracks oriented

* Corresponding author.
** Corresponding author.
E-mail addresses: yingchun_li@dlut.edu.cn (Y. Li), giselle02@163.com (C. Zuo).

Peer review under responsibility of Institute of Rock and Soil Mechanics, Chinese Academy of Sciences.

https://doi.org/10.1016/j.jrmge.2025.06.010

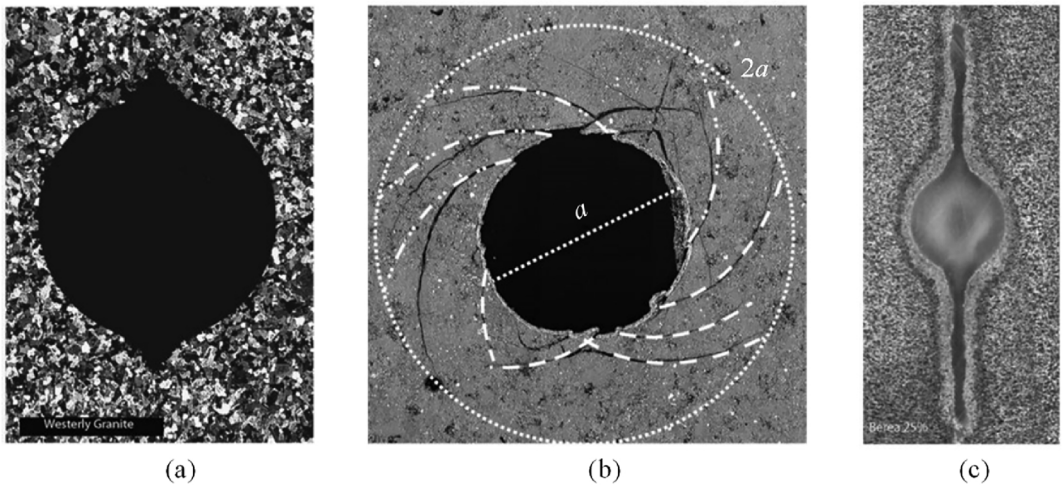

Fig. 1. Borehole deformations of different cross-sections: (a) V-shaped breakouts in Westerly granite, (b) spiral-shaped breakout in black shale (where '*a*' is the borehole diameter), and (c) slot-shaped breakouts in Berea sandstone.

parallel to the far-field principal stress, culminating in layer-by-layer flaking that yields V-shaped damage. Spiral failures occur when shear failure zones spiral outward along the borehole wall without causing immediate collapse. Groove failures typically result from compressive processes and grain rearrangement, generating narrower yet stable damage zones that often span only a few grain diameters in thickness.

While field and laboratory observations have contributed to macroscopic perspectives, a good understanding of microscopic fracture mechanisms of borehole breakouts remains elusive. Numerical modeling methods, broadly categorized into continuum and discontinuum approaches, have proven instrumental in shedding light on these micromechanical processes (Yousefian et al., 2020). On the continuum side, significant work includes boundary element method (Zheng et al., 1989) and CWFS (cohesion weakening friction strengthening) model (Hajiabdolmajid et al., 2002). Zhu et al. (2005) employed the RFPA (rock failure process analysis) code to simulate fracturing of heterogeneous rocks. Zhu and Bruhns (2008)examined how rock mass heterogeneity influences damage initiation. Nonetheless, continuum models face inherent challenges when capturing discontinuous processes, prompting the development of particle-based discontinuum approaches (Yazdani et al., 2024). Noteworthy contributions include PFC2D (particle flow code in two dimensions) simulations (Fakhimi et al., 2002), investigations of grain breakage (Lee et al., 2016), and analyses of anisotropic effects (Lan et al., 2013; Duan and Kwok, 2016) introduced a discrete element model (DEM) incorporating meso-scale heterogeneity, illuminating thermomechanical influences on damage evolution. Despite these methodological advances, borehole breakout remains a multifaceted phenomenon governed by in situ stress states, material properties, borehole size, and support measures (Brudy and Zoback, 1999; Zhang, 2013). While progress has been made in elucidating formation mechanisms—especially concerning rock heterogeneity—a critical aspect still requiring further exploration is the detailed mechanical response, including stress evolution and crack development of heterogeneous rocks under the impacts of varying confining pressures. Addressing these knowledge gaps is key for more reliable drilling designs, higher safety, and improved in-situ stress analyses (Lin et al., 2020a; Xiang et al., 2023).

Herein, we established a DEM-based modeling that embraces the micromechanical heterogeneity of grain contacts to reproduce typical borehole breakouts in laboratory-tested red sandstone. The heterogeneity was implemented by assigning micromechanical properties following the classic Weibull distribution to grain contacts. We strictly calibrated the heterogenous DEM model against laboratory measurements and further conducted systematical modeling to examine how micromechanical heterogeneity, in-situ stress and borehole geometry affect the macroscopic phenomenon.

2. Experimental study

2.1. Fundamental rock property tests

Red sandstone samples for this study were sourced from a mine in Hunan Province, China. They exhibited ochre red with fine mineral grains and little surface weathering. Following ISRM suggestions (Culshaw, 2015), cylindrical samples were prepared in two sizes: 100 mm height × 50 mm diameter for uniaxial and triaxial compression tests, and 25 mm height × 50 mm diameter for Brazilian tension tests. The red sandstone sample has a density of 2380 kg/m^3. Scanning Electron Microscopy (SEM) examination shows a heterogeneous structure comprising irregular mineral grains with intervening pores and microcracks (Fig. 2a). The grain size ranges from 0.3 to 270 μm with a median value of 101.9 μm (Fig. 2b). X-ray Diffraction (XRD) analysis identified quartz, feldspar, calcite, hematite, mica, and clay as the primary mineral constituents (Fig. 2c). Computed Tomography (CT) scan reconstructed the three-dimensional (3D) pore geometry and revealed a porosity of 8.94 % (Fig. 2d).

To quantify the rock's mechanical properties, a series of fundamental laboratory tests was conducted. These included uniaxial compression, triaxial compression (confining pressures of 5 MPa, 15 MPa and 25 MPa) and Brazilian tension tests. Table 1 summarizes the resulting data—uniaxial compressive strength, elastic modulus, Poisson's ratio, friction angle, and cohesion. These parameters informed both the borehole breakout experiments and the subsequent calibration of the DEM modeling realized by the universal distinct element code (UDEC) (Itasca, 2019).

2.2. Borehole breakout experiments

For the borehole breakout tests, three groups of thick-walled cylindrical samples (labeled Z10, Z15, and Z20) are prepared by

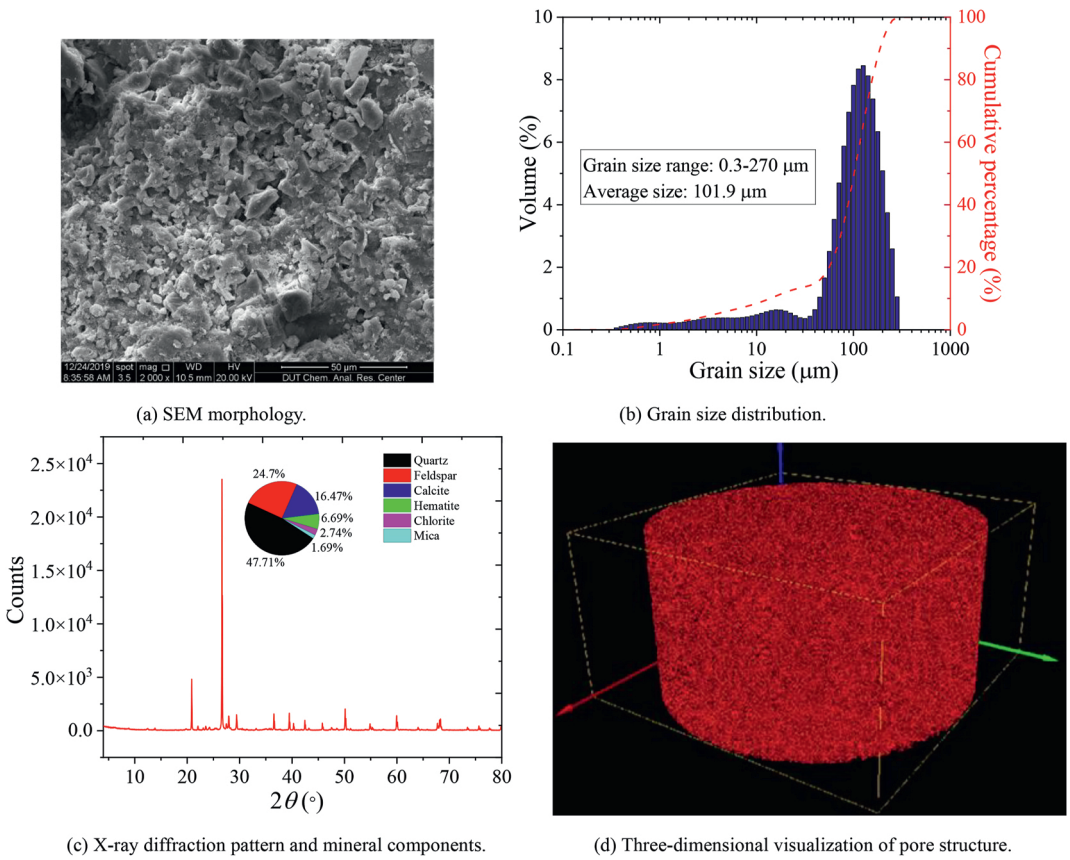

(a) SEM morphology.

(b) Grain size distribution.

(c) X-ray diffraction pattern and mineral components.

(d) Three-dimensional visualization of pore structure.

Fig. 2. Microstructural and mineralogical characterization of sandstone samples.

Table 1
Mechanical properties of red sandstone.

Uniaxial compressive strength (MPa)	Tensile strength (MPa)	Elastic modulus (GPa)	Poisson's ratio	Internal friction angle (°)	Cohesion (MPa)
69.34	3.87	13.67	0.227	38	17.8

drilling axial holes of 10 mm, 15 mm, and 20 mm in diameter into 50 mm × 100 mm cylinders (Fig. 3a). Hydrostatic loading experiments were then conducted using an MTS815 rock mechanics system at the Rock Mechanics and Geohazards Experimental Center, Shaoxing University, China. Each sample was first loaded at a constant rate of 2 MPa/min until borehole failed and subsequently unloaded at a constant rate of 4 MPa/min. Fig. 3b displays three distinct loading stages based on the hydrostatic pressure–circumferential strain curves. The initial stage features a nonlinear increase that reflects the gradual closure of pre-existing microcracks, followed by a linear growth where strain increases proportionally with stress, indicating stable elastic deformation. At the final failure stage, apparent inflection points and rapid increase in circumferential strain mark the onset of borehole breakout. Beyond this point is termed critical hydrostatic pressure (P^*), and the sample undergoes structural instability and accelerates interior deformation around the borehole. A negative correlation appears between borehole diameter and critical hydrostatic pressure. With borehole diameters of 10 mm, 15 mm, and 20 mm, the critical hydrostatic pressure dropped from 120.1 MPa to 82.6 MPa—a 31 % decrease—while the circumferential strain at failure rose slightly from 0.53 % to 0.60 %.

Post-failure examination employed nanoVoxel-4000 series CT scanning (190 kV and 30 μA, achieving a high resolution of 27.78 μm) to visualize the borehole breakout patterns using both axial and cross-sectional images. For Z10 sample (diameter D = 10 mm), the axial CT scan (Fig. 4a) reveals multiple cracks aligned with the borehole axis, causing non-uniform damage. Central regions demonstrated pronounced spalling that created a spindle-shaped cavity with maximum width near the borehole's midpoint, suggesting that breakout initiated around the borehole center and expanded outward. Cross-sectional CT scans are taken at five positions: the sample center and distances of D = 10 mm and 20 mm from either end (Fig. 4b). These sections show increasing breakout span and depth toward the sample's center, forming nearly symmetrical V-shaped failure zones on opposite sides of the borehole. Slight angular deviations appear between sections b-b' and c-c', indicating the breakout path may not perfectly align with the borehole axis. Similar V-shaped patterns appear in Z15 (D = 15 mm) and Z20 (D = 20 mm) samples (Fig. 5), confirming that despite potential boundary effects in larger diameter samples, the fundamental failure mechanism remains consistent across all tested configurations.

Total CT observations across different borehole diameters revealed a consistent failure process. Initially, tensile microcracks form parallel to the borehole in two opposing zones, facilitated by the rock's intrinsic heterogeneity. Upon further loading, these cracks progressively widen and coalesce; when they intersect the

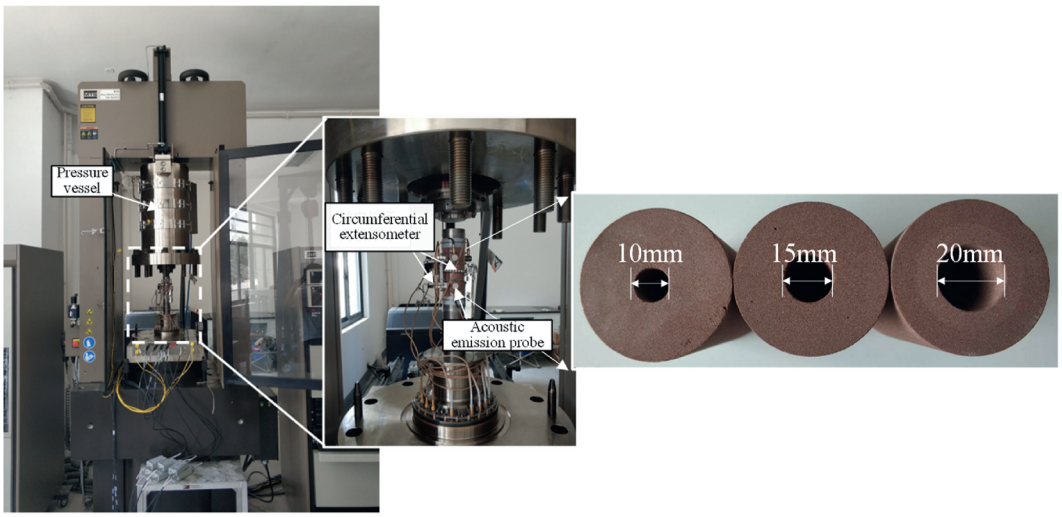

(a) The MTS815 rock mechanics system and prepared thick-walled cylindrical samples.

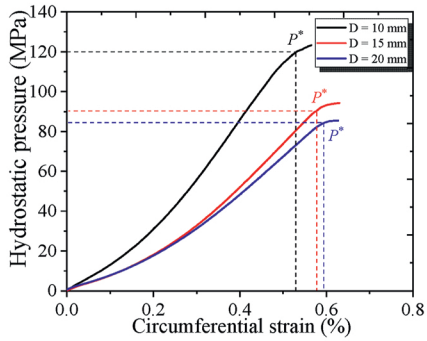

(b) Hydrostatic stress - circumferential strain curve of borehole samples.

Fig. 3. Experimental system and hydrostatic compression tests on sandstone borehole samples. *D* is the hole diameter.

borehole boundary, thin rock slices detach. At their deeper ends, shear cracks develop, promoting spalling and stress redistribution. New cracks arise consequently behind the newly formed borehole boundary, causing incremental detachment of smaller fragments until a well-defined V-shaped failure zone emerges. These findings align with previous studies on Berea and Tennessee sandstones under hydrostatic loading (Ewy and Cook, 1990; Cuss et al., 2003).

3. Numerical modeling

3.1. DEM modeling

Unlike PFC, UDEC interprets the brittle material as an assembly of deformable blocks, namely the soft grain approach that allows the deformation of grain itself—a feature typically absent in PFC's conventional rigid grain approach. The elastic deformation of a grain is governed by its elastic modulus and Poisson's ratio. UDEC generates a two-dimensional grain structure using the Voronoi tessellation that creates *n*-sided polygonal grains around randomly distributed seed points. Each grain occupies the region closest to its respective seed point, maintaining internal integrity while interacting with neighboring grains via constitutive relationships (Ghazvinian et al., 2014) (Fig. 6):

$$\Delta\sigma_n = -k_n \Delta u_n \tag{1}$$

$$\Delta\tau_s = -k_s \Delta u_s^e \tag{2}$$

where $\Delta\sigma_n$ and Δu_n represent the normal stress and displacement increments, respectively; $\Delta\tau_s$ denotes the shear stress; k_n and k_s are the stiffness coefficients; and Δu_s^e is the elastic component of shear displacement increment.

Crack occurs when stresses exceed contact strength thresholds, i.e. tensile failure occurs to the contact once its tensile strength is surpassed, whereas shear failure constrains shear stress to $\tau_s = \text{sign}(\Delta u_s)\tau_{max}$, where sign(·) is the sign function that returns +1 or −1 based on the direction of displacement, Δu_s is the total shear displacement increment and τ_{max} is the peak shear strength of a contact (i.e. contact cohesion plus normal stress multiplying tangent of contact friction angle). After the contact fails in shear, its shear strength drops immediately to the residual value with the residual friction angle without any cohesion.

Rock grain and contact parameters were calibrated using laboratory tests described in Section 2, establishing the foundation for borehole breakout simulations. Seven key parameters were identified: elastic modulus and Poisson's ratio for grains, and normal stiffness, tangential stiffness, friction angle, cohesion, and tensile strength for contacts. A sensitivity analysis was first conducted in Section 3.2 to understand how these contact parameters influenced the mechanical behavior. The five contact parameters were then calibrated by comparing numerical results to experimental measurements from compression and tension tests as detailed in Section 3.3. For computational efficiency, we employed

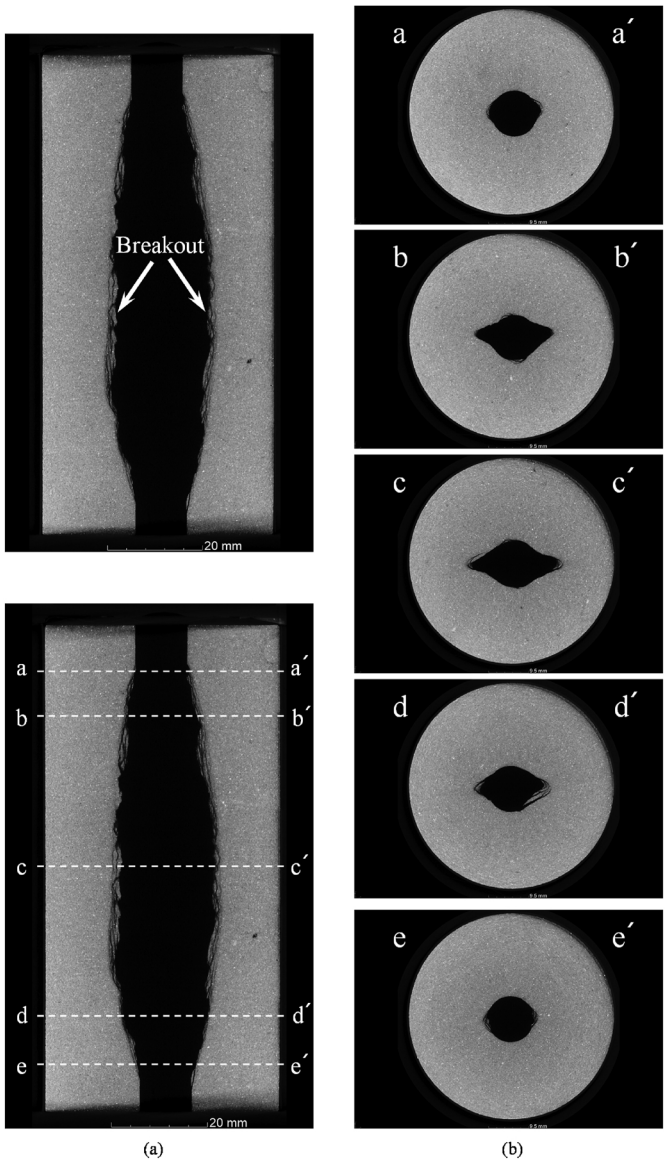

Fig. 4. CT scans of borehole sample Z10: (a) axial images and right, and (b) cross-sectional images.

model scaling based on previous research (Lan et al., 2010). The original 2D cylindrical sample (100 mm × 50 mm with 5163 grains) for compression tests and disk sample (50 mm diameter with 2042 grains) (Fig. 7a) for Brazilian tests are reduced to 0.8 (4176 grains), 0.5 (2525 grains), and 0.4 (2068 grains) of their original dimensions while maintaining the average grain size at 0.2 mm. This grain size was selected to balance computational efficiency with accurate representation of failure mechanisms (Ding et al., 2014). All scaled models show similar pre-peak stress-strain behavior with only minor post-peak variations (Fig. 7b), allowing us to select the 0.5-scale model for subsequent simulations. Samples were loaded between frictionless platens at a constant strain rate of 10^{-5} mm/step to maintain quasi-static conditions (Gao and Stead, 2014). Post-failure behavior was modeled by setting residual tensile strength and cohesion to zero while maintaining a residual friction angle of 10° (Justo et al., 2022). Macroscopic stress was calculated by averaging grain stresses, with axial and radial strains derived from displacement records.

3.2. Sensitivity analysis

To streamline calibration against laboratory data, we first analyzed the contact parameters. This analysis identified how contact parameters impact the model's macroscopic mechanical response, revealing which parameters strongly influence specific overall behaviors and thus guiding the subsequent calibration procedure.

3.2.1. Contact stiffness

Previous studies show that a rock model's macroscopic elastic properties (Young's modulus and Poisson's ratio) are strongly influenced by the normal stiffness (k_n) and shear stiffness (k_s) of inter-grain contact (Kazerani and Zhao, 2010; Gao and Stead, 2014; Ghazvinian et al., 2014). In this study, we conducted two sets of uniaxial compression tests to assess this impact. In the first set, we held $k_s/k_n = 0.5$ (Gao et al., 2016) and varied both k_n and k_s from 4×10^4 GPa/m to 1×10^5 GPa/m. This means both parameters were varied simultaneously while maintaining their fixed ratio. In the second set, we set $k_n = 6.8 \times 10^4$ GPa/m and gradually raised k_s to yield k_s/k_n ratios ranging from 0.125 to 0.667. Results from the first set (Fig. 8a) indicate that a higher stiffness produces an increased Young's modulus, with the growth rate diminishing at the upper limits of the stiffness range. Only a slight increase was observed in Poisson's ratio, signifying relatively low sensitivity to changes in stiffness under a constant k_s/k_n. In the second set (Fig. 8b), raising the k_s/k_n ratio lowers Poisson's ratio from 0.491 to 0.196 before it stabilizes near 0.2. Meanwhile, Young's modulus continued to rise with an increasing k_s/k_n, underscoring the importance of shear stiffness in defining the elastic response.

3.2.2. Contact cohesion

Under compressive loading, shear failure is the predominant failure mechanism in rock and is primarily controlled by contact cohesion (C^c) and friction angle (φ^c). These parameters strongly influence both uniaxial and triaxial compressive strength. To evaluate the influence of C^c on sample strength, we performed triaxial compression tests at four levels of C^c (=18 MPa, 24 MPa, 30 MPa, and 36 MPa), keeping all other parameters constant. Each level was tested under confining pressures of 0 MPa, 5 MPa, 10 MPa, and 15 MPa. For each set of triaxial test results, the corresponding Mohr circles are plotted, and a linear Mohr-Coulomb strength envelope is fitted (see Fig. 9a). From the interception and slope of this envelope, the sample cohesion (C^s) and the friction angle (φ^s) were determined. Analysis of how these macroscopic parameters change with varying contact cohesion (C^c) (Fig. 8c) reveals two key findings: (a) the relationship between the contact cohesion (C^c) and the sample's friction angle (φ^s) is approximately constant, exhibiting only minor deviations (within 3 %) at $C^c = 18$ MPa, implying that φ^s remains nearly constant at different C^c values; and (b) the sample cohesion (C^s) increases linearly with rising contact cohesion C^c. As C^c increases from 18 MPa to 36 MPa, C^s grows from 13.5 MPa to 24.8 MPa-a total increase of ~83.7 %. These observations confirm that contact cohesion is the dominant factor controlling sample cohesion.

3.2.3. Contact friction angle

We generated four sets of numerical samples with different contact friction angles ($\varphi^c = 30°$, 34°, 38°, and 42°) while keeping other parameters unchanged. These samples undergo the same triaxial compression tests introduced in Section 3.2.2, and the Mohr circles and strength envelopes are shown in Fig. 9b. Fig. 8d suggests that:

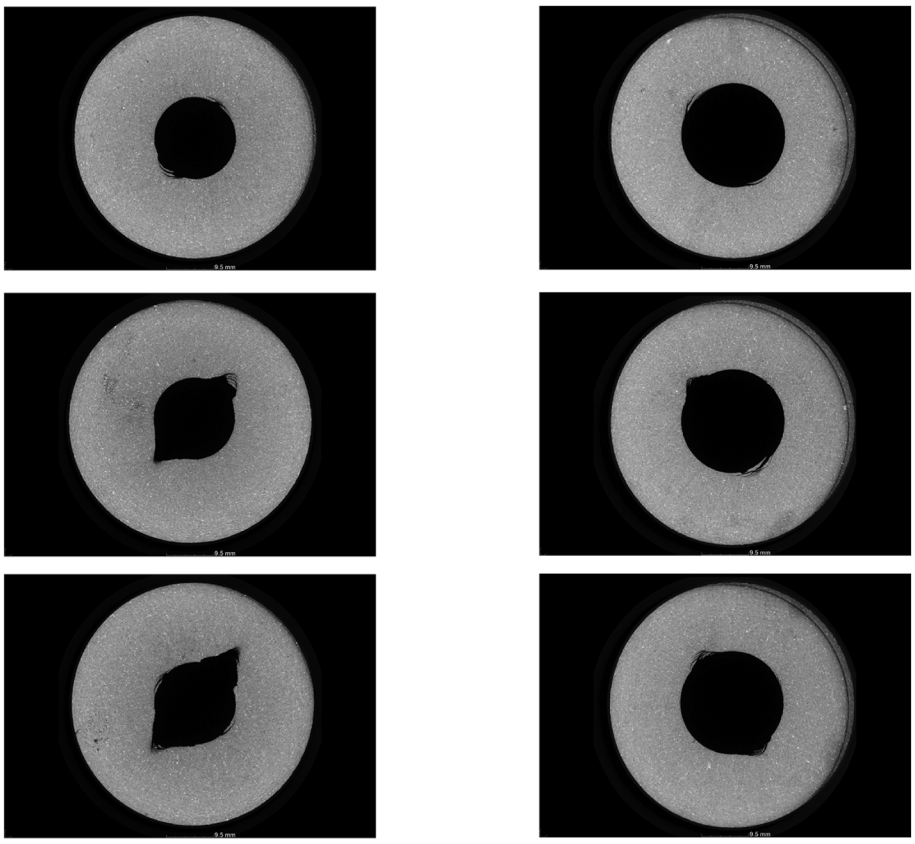

Fig. 5. CT scans of borehole sample cross-sections: (a) Z15, and (b) Z20.

(1) The sample friction angle (φ^s) exhibits a strong positive correlation with φ^c. An increase in φ^c from 30° to 42° (~40 %) leads φ^s to rise from 31° to 44° (~42 %); and
(2) The sample cohesion (C^s) is relatively insensitive to φ^c, decreasing only slightly from 20 MPa to 18.5 MPa as φ^c increases. Thus, sample cohesion is influenced predominantly by contact cohesion, while the sample's friction angle is primarily governed by the contact friction angle.

3.2.4. Contact tensile strength

We also explored the influence of contact tensile strength on overall tensile strength by conducting Brazilian splitting tests. Four numerical models were created with contact tensile strengths varying from 5 MPa to 8 MPa. As shown in Fig. 8e, the sample tensile strength shows a marked increase when the contact tensile strength rises, indicating a direct proportional relationship between these two parameters.

3.3. Calibration

The two grain parameters were derived from the average elastic properties of the red sandstone. Guided by the preceding sensitivity analysis, we calibrated the five contact parameters through the following steps:

(1) Determine the elastic modulus and Poisson's ratio of grains and contact stiffnesses (normal and tangential) by correlating with laboratory measurements of uniaxial and triaxial compression tests.

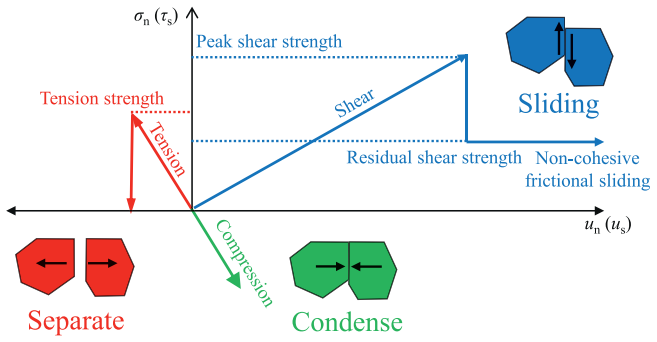

Fig. 6. Contact constitutive model (σ_n and σ_s denote the normal stress and shear stress, respectively; and u_n and u_s represent the normal displacement and shear displacement, respectively).

(2) Tune contact cohesion and friction angle by comparing to laboratory measurements of triaxial compression results.
(3) Calibrate contact tensile strength through laboratory measurements of Brazilian tension tests.

In this study, we first determined the grain elastic modulus and Poisson's ratio through trial-and-error correlating with the experimentally determined stress-strain relationships (Oh et al., 2017). These two elastic properties were evaluated at 17.73 GPa and 0.2, respectively. Selecting an appropriate grain size is crucial. While ideally it should match the real mineral grain size,

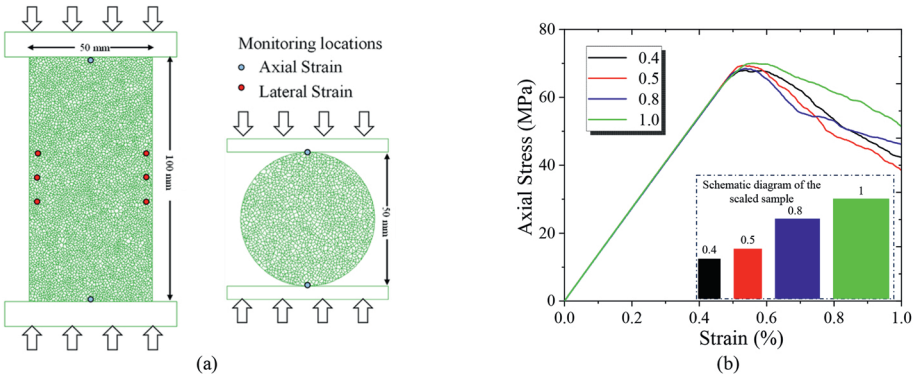

Fig. 7. Numerical model configuration and scale effect validation: (a) Geometrical configuration of UDEC models for contact parameter calibration: uniaxial/triaxial compression and Brazilian tension tests; and (b) scale analysis of stress-strain behavior under uniaxial compression.

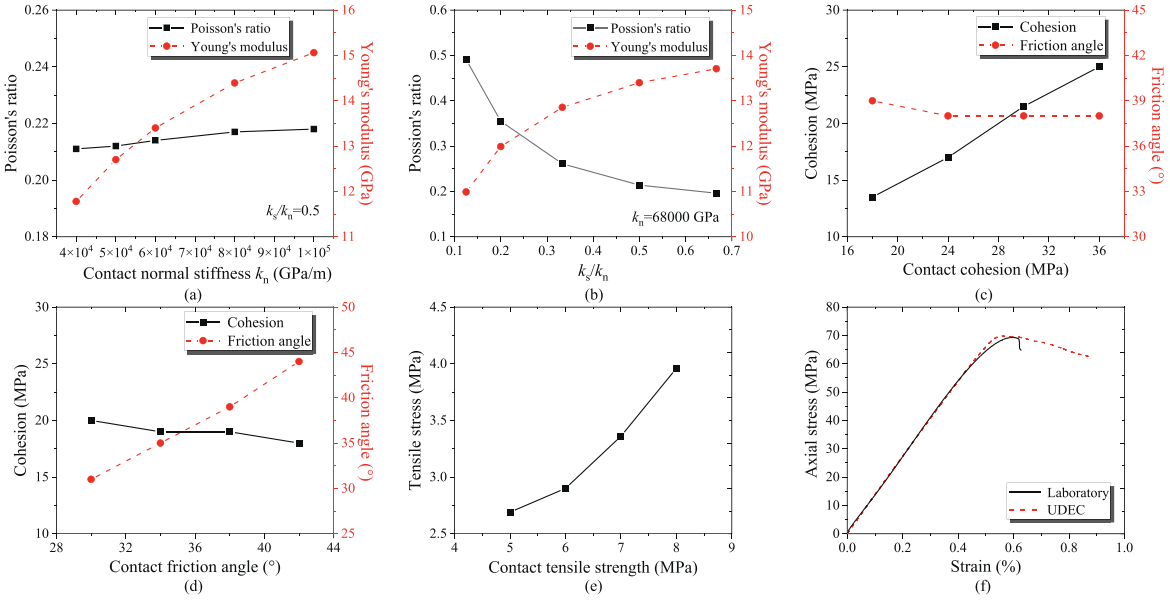

Fig. 8. Sensitivity analysis on contact parameters: (a) Influence of normal contact stiffness value on macroscopic elastic properties, (b) Effect of shear-to-normal (k_s/k_n) stiffness ratio on macroscopic elastic properties, (c) Impact of contact cohesion on macroscopic cohesion and internal friction angle, (d) Impact of contact friction angle on macroscopic cohesion and internal friction angle, (e) Relationship between contact tensile strength and macroscopic tensile strength, and (f) Comparison of stress-strain curves between numerical simulation and laboratory tests (uniaxial compression).

computational constraints necessitate using larger grain sizes. The chosen grain size balances the need to capture fracturing mechanisms with modeling efficiency. After finalizing the parameters (Table 2), we numerically performed uniaxial compression tests on simulated rock samples. These simulations closely matched the experimental stress-strain curves (Fig. 8f).

3.4. Contact heterogeneity implementation

We utilized the embedded programing language, FISH scripts (Itasca, 2019) in UDEC to assign the contact parameters according to a Weibull distribution, allowing each contact to have randomly allocated properties (Tang et al., 2000). This approach reproduces the inherent heterogeneity of natural rock. The probability density distribution (PDF) of the Weibull function is given by (Zheng et al., 1989; Tang et al., 1998):

$$f(u)=\frac{m}{u_0}\left(\frac{u}{u_0}\right)^{m-1}\exp\left[\left(-\frac{u}{u_0}\right)^{m}\right] \tag{3}$$

where $f(u)$ represents the probability density function for a given mechanical parameter, u is the specific value of that parameter for an element, u_0 is the mean value of this parameter across all elements, and m is the shape parameter (also termed homogeneity coefficient in this study). Higher m values correspond to more uniform materials (Fig. 10a).

Our investigations focus on rock mechanical responses solely induced by contact heterogeneity. Hence, numerically simulated samples share the same grain geometry, arrangement, and properties to avoid disturbances from geometric or elastic heterogeneity. Given u and m, each simulation still generates a unique spatial distribution of contact properties, as parameter values are assigned randomly. To examine this variability, we ran four

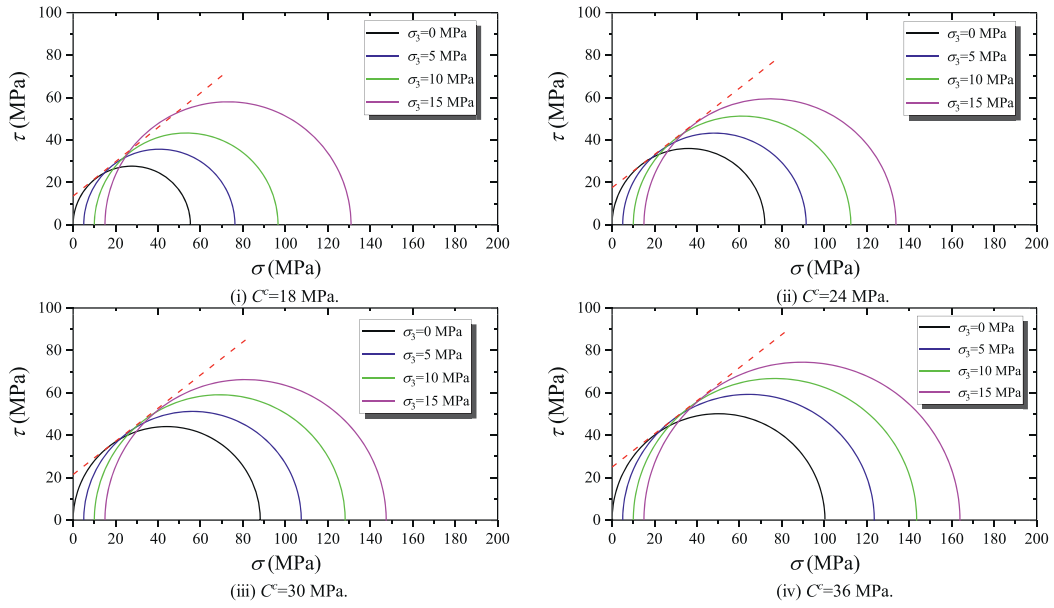

(a) Contact cohesion (18-36 MPa).

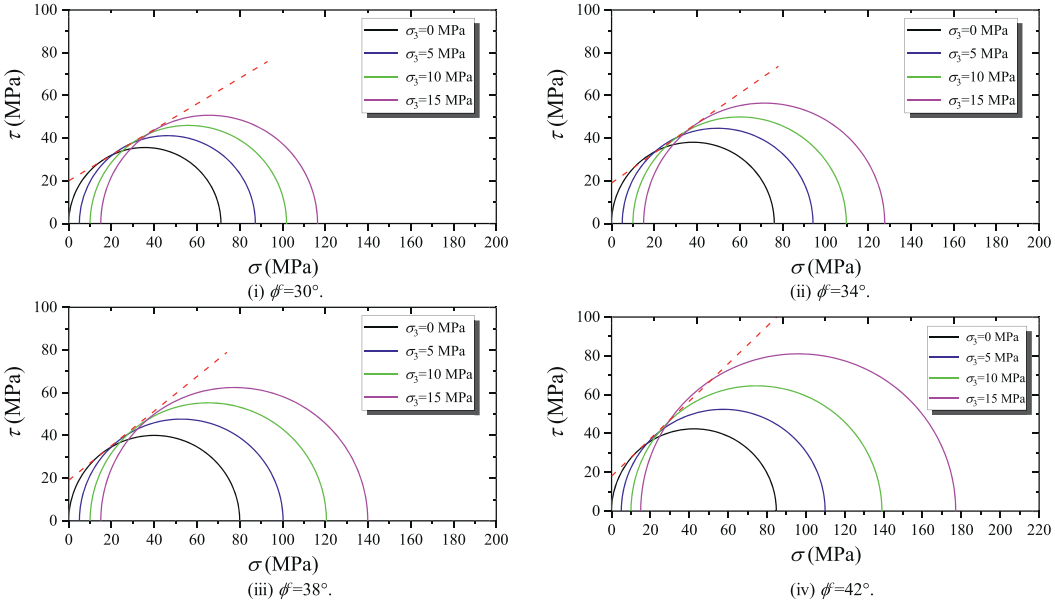

(b) Contact internal friction angle (30°-42°).

Fig. 9. Mohr-Coulomb failure envelopes for various contact parameters.

Table 2
Calibrated micromechanical parameters of homogeneous sandstone sample.

Type of parameters		
	Elastic modulus (GPa)	17.73
	Poisson's ratio	0.2
Contact parameters	Normal stiffness (GPa/m)	68,000
	Tangential stiffness (GPa/m)	30,000
	Friction angle (°)	38
	Residual friction angle (°)	10
	Cohesion (MPa)	24
	Tensile strength (MPa)	8

uniaxial compression tests on samples whose contact parameters follow the same Weibull distribution (u and m). Their failure patterns showed minor variations and the overall stress-strain responses were nearly identical, indicating that different random spatial distributions of the same u and m cause only minimal effects on mechanical performance (Fig. 10b).

We investigated rock heterogeneity effects through numerical-simulated uniaxial compression tests using samples of varying Weibull homogeneity coefficients (m = 1.5, 3.5, and 10, representing increasing rock uniformity) compared with a benchmark homogeneous model ($m \to \infty$). Since in the FISH programing, it is impossible to assign the homogeneity coefficient (m) with an infinite large ∞, we employed a very high value of $m = 1 \times 10^5$ to achieve the simulation of the homogenous material (Wang et al., 2024; Yu et al., 2025). To exclude the geometrical distinction generated by the Voronoi algorithm, we adopted a two-step numerical modeling procedure. We first saved the UDEC file of the Voronoi-generated geometrical model. Then we restored the

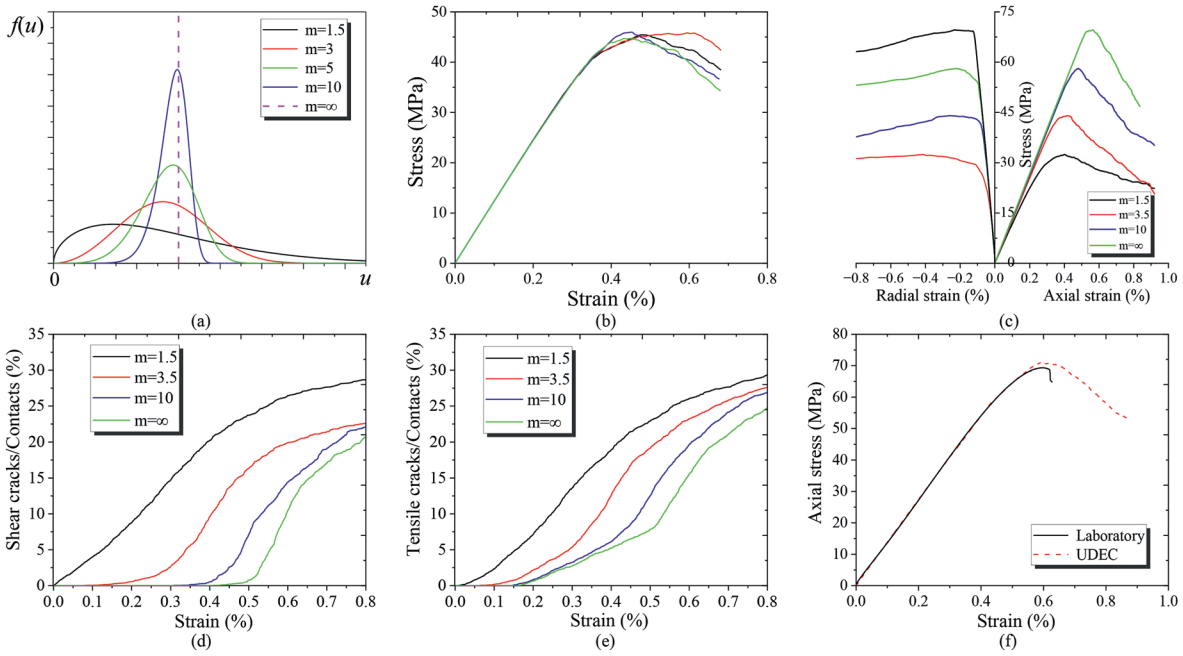

Fig. 10. Effects of contact heterogeneity on rock mechanical behavior: (a) Weibull probability density functions with varying homogeneity coefficients, (b) stress-strain curves for different random spatial distributions ($m = 3.5$), (c) influence of homogeneity coefficient on stress-strain behavior, (d) evolution of tensile crack density under different m values, (e) evolution of shear crack density under different m values, and (f) comparison between heterogeneous model and experimental results.

above file and assigned mechanical properties of values generated by the Weibull function of different homogeneity coefficients to grain contacts of the geometrical model. It means that the numerical models of different homogeneity coefficients share the same grain geometry and topology. Additionally, to avoid random numbering in the Weibull function of the same homogeneity coefficient and incur slight differences in pre-peak softening and post-peak behavior (Fig. 10b), the values generated by the Weibull function are fixed and then assigned these values to contact mechanical properties in UDEC. In this manner, both the geometrical and mechanical properties of grains and contacts can be kept unvaried. As presented in Fig. 10c, decreasing m (i.e. lower the rock homogeneity) significantly lowers the peak strength (from 69.87 MPa to 32.76 MPa, ~53 % reduction) and slightly reduces the elastic modulus (from 13.67 GPa to 11.91 GPa, ~13 % reduction). The axial stress-axial strain relationships suggest that a lower m also increases nonlinear deformation prior to peak stress and results in a more gradual post-peak decline, suggesting a progressive failure process that is also signified by the mild shear/tensile crack evolution over axial loading (Fig. 10d and e). In contrast, a larger m produces a sudden post-peak drop, indicating a more brittle failure. Fig. 10d and e illustrates the development of tensile and shear cracks during uniaxial compression for different m. A smaller homogeneity coefficient (m) triggers earlier initiation of tensile and shear cracks, along with smoother crack-growth curves and higher crack densities at failure. For $m = 1.5$, cracks develop throughout much of the sample by the time of final rupture, and more than 20 % of contacts fail in shear. As m increases, the final crack density decreases, especially for shear cracks, because they readily join with tensile cracks to form localized bands of damage. As a result, the macroscopic stress-strain response shows nearly linear deformation and sharper failure, indicating a more brittle nature. The spatial distribution of cracks, shown in Fig. 11, varies with the prescribed homogeneity coefficient. At $m = 1.5$, crack manifests nearly uniformly throughout the sample. When $m = 3.5$, the pattern consists primarily of several vertical tensile cracks with shorter shear cracks. At $m = 10$, cracking concentrates at the sample corners, forming an X-shaped pattern. In the homogeneous case ($m \to \infty$), the sample develops significantly fewer cracks overall, with discrete cracking rather than distributed damage.

We adopted a homogeneity coefficient $m = 3.5$ for the red sandstone sample (Li et al., 2020). This parameter influences the macroscopic mechanical behavior, necessitating recalibration of contact parameters according to procedures in Section 3.3. Table 3 lists these calibrated values, which represent mean values (u_0) in the Weibull distribution, with actual contact properties varying spatially throughout the sample. Uniaxial compression tests (Fig. 10f) validate our approach, showing good agreement between the heterogeneous model and experimental observations. While some discrepancy exists in the post-peak behavior—attributed to differences between idealized numerical softening and the rapid unloading kicking of stiff testing systems—the heterogeneous model more accurately captures pre-peak nonlinear deformation compared to homogeneous simulations.

4. Numerical simulation of borehole breakout

4.1. Numerical configuration and boundary conditions

Fig. 12a and b shows the simulated rock sample and the loading path for the borehole breakout simulations. Each simulation was performed on a square sample (50 mm × 50 mm) containing a centrally located borehole ($D = 10$ mm), constructed from polygonal grains with an average size of 0.2 mm. Previous studies (Haimson, 2007; Meier et al., 2013) indicate that borehole damage typically extends to about twice the borehole diameter; hence, the region within this distance (white dashed cube area in Fig. 12a) is discretized to explicitly capture failure mechanisms. The surrounding area was modeled as elastic blocks to efficiently represent far-field rock behavior and provide smooth boundary conditions (loading and displacement) for the closer discretized zone. In each simulation, principal horizontal stresses σ_Y and σ_X are

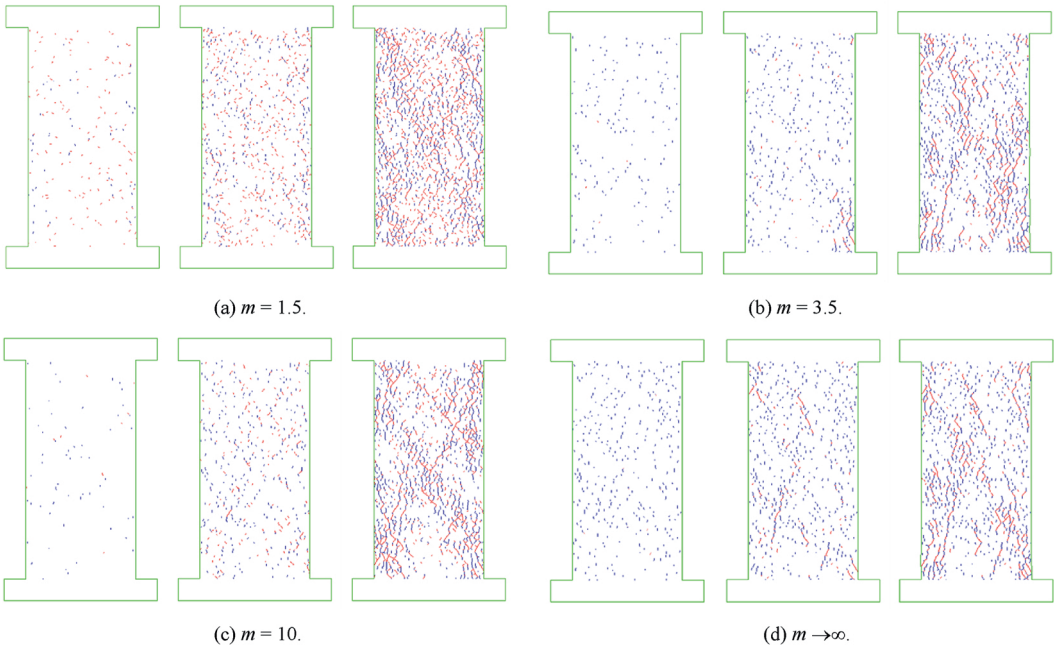

Fig. 11. Spatial distribution of tensile crack (red) and shear crack (blue) under uniaxial compression for different homogeneity coefficients.

Table 3
Calibrated mean values (u_0) for Weibull-distributed micromechanical parameters in heterogeneous sandstone model of homogeneity coefficient at 3.5.

Grain parameters		Contact parameters					
Elastic modulus (GPa)	Poisson's ratio	Normal stiffness (GPa/m)	Tangential stiffness (GPa/m)	Friction angle (°)	Residual friction angle (°)	Cohesion (MPa)	Tensile strength (MPa)
17.73	0.2	4.2×10^5	1.6×10^5	30	10	45	8

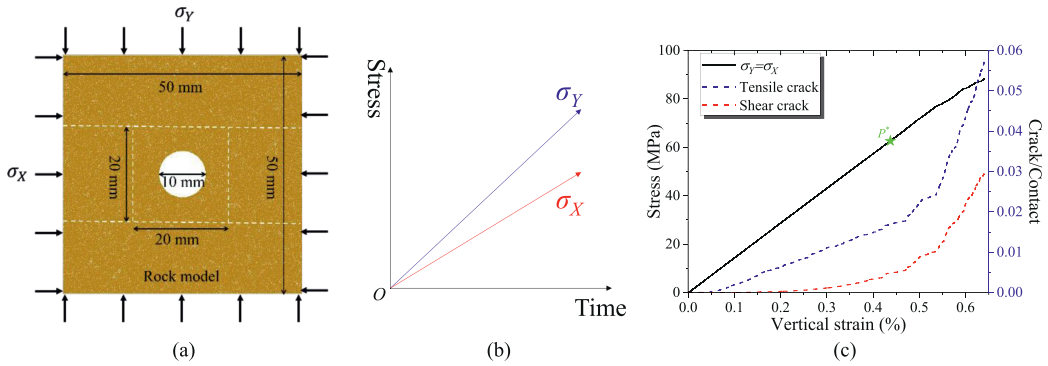

Fig. 12. Numerical setup and mechanical response of borehole breakout simulation: (a) Heterogeneous UDEC model geometry and discretization, (b) applied stress loading path, and (c) evolution of stress-strain relationship and crack density under hydrostatic loading.

applied simultaneously, while maintaining a constant lateral pressure coefficient K (Fig. 12b). Borehole breakout initiation is identified by a distinct change in slope of the crack count curve signifying accelerated microcrack formation (Fig. 12c). Throughout loading, we calculated sample stress by averaging grain stresses, measured axial and radial strains from monitored displacement, and tracked both crack initiation and damage zone evolution.

4.2. Borehole breakout under hydrostatic pressure

An initial borehole breakout simulation was conducted with a homogeneity coefficient $m = 3.5$ and $K = 1$ (hydrostatic conditions, $\sigma_Y = \sigma_X$). Fig. 12c shows the stress-strain curve and the ratio of cracked contacts to total contacts. During the initial linear-elastic stage (<60 MPa), both tensile and shear crack form gradually but remain mostly independent. Beyond ~60 MPa, crack growth accelerates, and interactions between tensile and shear cracks cause grain spalling around the borehole. When the vertical stress reaches the critical hydrostatic pressure (P^* = ~63 MPa), shear cracking becomes more prevalent, intersecting with tensile cracks and creating a surge in the crack growth curves. This surge induces fluctuations in the stress-strain response and signals borehole breakout.

Fig. 13 presents stress distribution, crack distribution and

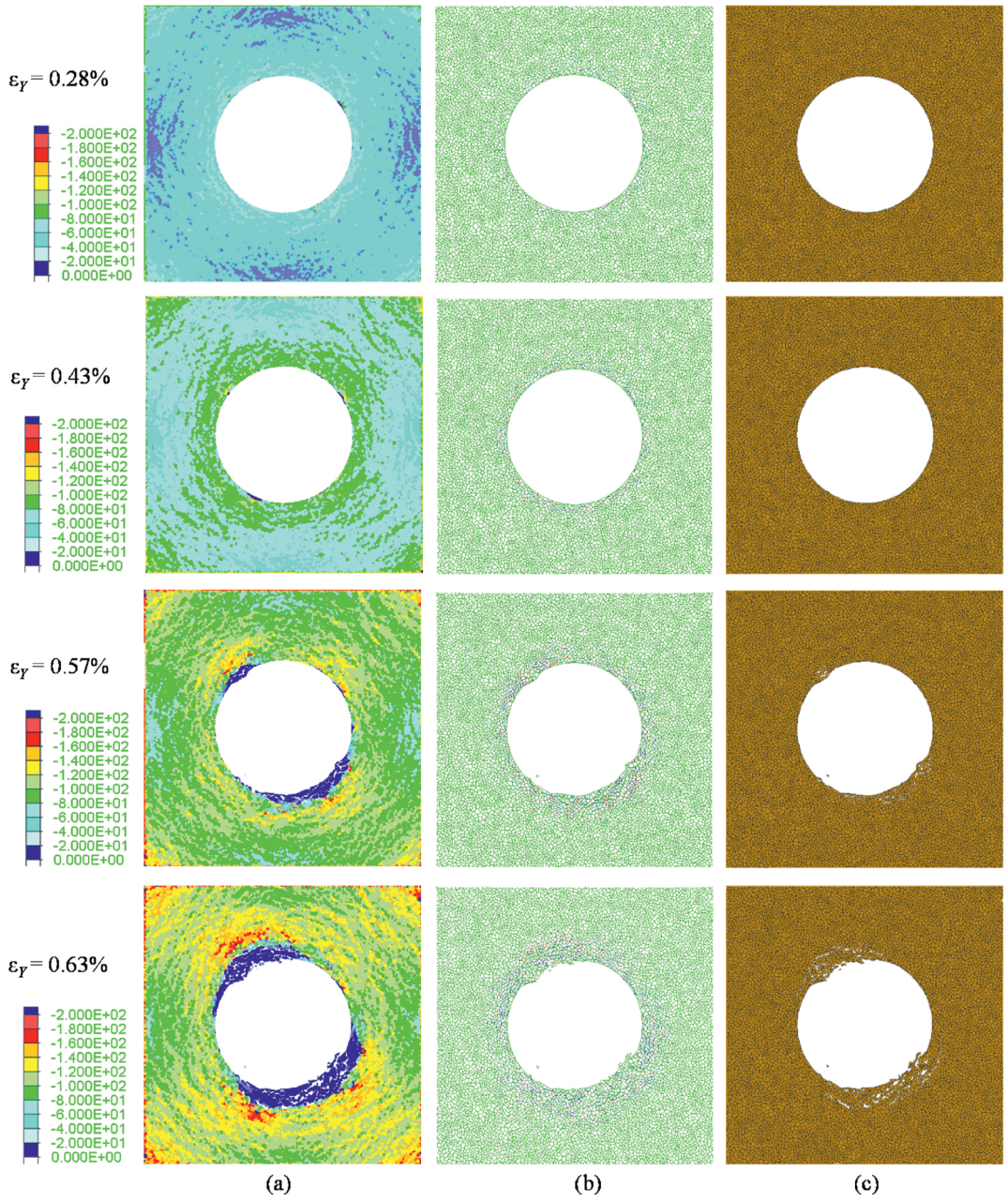

Fig. 13. Progressive development of borehole breakout under hydrostatic loading conditions: (a) Maximum principal stress, (b) crack evolution, tensile cracks are blue, shear crack are red, and (c) breakout geometry.

breakout geometry at different loading stages. By ε_Y = 0.28 %, localized stress concentrations due to rock heterogeneity produce scattered initial cracks near the borehole, mostly tensile and parallel to the borehole wall. By ε_Y = 0.43 %, many tensile cracks penetrate deeper into the rock, yet remain isolated and parallel. Only a fraction of them, close to the borehole surface, connect via shear cracks and cause block spalling. By ε_Y = 0.57 %, failure zones preferentially appear on opposite sides of the borehole, where shear cracks link with existing tensile cracks at an angle, peeling off thin rock plates. This spalling triggers further cracking, enlarging the failure zone. Eventually, at ε_Y = 0.63 %, a symmetrical V-shaped failure zone is formed. Quantitative analysis using the geometry measurement (Lin et al., 2020b) yields breakout dimensions (angular span of 75.1° and depth of 7.15 mm) in close agreement with experimental measurements (angular span of 69.3° and depth of 6.64 mm in Fig. 14).

4.3. Influence of far-field stress on borehole breakout

The values K = 0.25–2.0 were selected to evaluate how far-field stress conditions affect borehole breakout development, ranging from highly anisotropic (K = 0.25 or 2.0) to isotropic (K = 1) conditions. Fig. 15 shows the stress-strain curves and crack ratios, and Fig. 16 illustrates the maximum principal stress and crack distributions at representative loading stages.

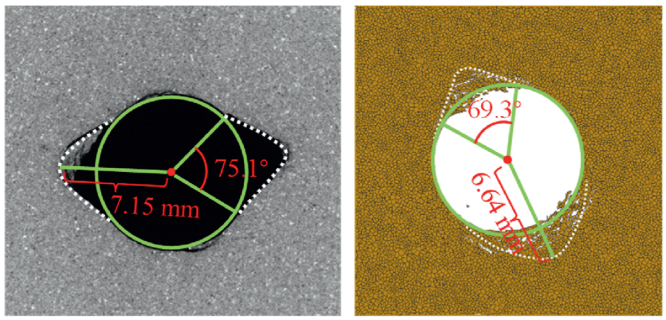

Fig. 14. Comparison of borehole breakout patterns between experimental and numerical results under hydrostatic loading ($K = 1$), showing a good agreement in the breakout geometry.

(1) At $K = 0.25$ (Figs. 15a and 16a), shear cracks appear around $\varepsilon_Y \approx 0.28$ % followed by a relatively steady growth of both crack types. Tensile cracks outnumber shear cracks, and their difference widens with loading. By $\varepsilon_Y \approx 0.58$ %, crack growth rates sharply increase, signifying breakout. Tensile cracks reach 4.4 %, with shear cracks at 0.5 %. A V-shaped, tensile-dominated failure zone then surrounds the borehole.
(2) At $K = 0.5$ (Figs. 15b and 16b), tensile and shear cracks appear at a strain level resembling that at $K = 0.25$, but breakout begins at $\varepsilon_Y \approx 0.6$ %. Although tensile cracks still dominate, the difference between tensile (~1.8 %) and shear (~0.4 %) cracks narrows. Multiple spalling points emerge around the borehole, eventually merging into a V-shaped failure zone on the right side of the borehole before extending to the opposite side.
(3) At $K = 0.8$ (Figs. 15c and 16c), the failure zone is larger than at lower K values, initiating at $\varepsilon_Y \approx 0.56$ % with tensile cracks at ~1.7 % and shear at ~0.5 %. At $K = 1$ (Figs. 15d and 16d), *breakout* occurs around $\varepsilon_Y \approx 0.47$ % under similar crack densities (tensile ~1.8 %, shear ~0.5 %).
(4) At $K = 1.25$ and $K = 2$ (Figs. 15e–f and 16e–f), the vertical strain at breakout declines, reflecting that deformation concentrates near the top and bottom of the borehole while the horizontal strain becomes dominant. Despite minor variations in crack density, symmetrical V-shaped failure zones still appear opposite each other in the direction of minimum horizontal principal stress.

Overall, while local heterogeneity affects specific crack pathways and geometries, far-field stress and its orientation primarily govern borehole breakout patterns.

4.4. Influence of heterogeneity on borehole breakout

To investigate the effect of rock heterogeneity, three numerical samples were created with homogeneity coefficients $m = 1.5$, 3.5, and 10. Their crack evolution and final failure patterns were analyzed at two different lateral pressure coefficients ($K = 1$ and $K = 0.5$).

(1) $K = 1$ and $m = 1.5$ (Figs. 17a and 18a): Highly heterogeneous samples exhibit lower overall strength. Shear cracks appear immediately upon loading, in addition to tensile cracks near the borehole. Throughout loading, shear cracks are more than tensile cracks, a pattern reversing that of more homogeneous samples. As loading continues, both crack types spread around the borehole, forming three major failure zones that surround the borehole.
(2) $K = 1$ and $m = 10$ (Figs. 17c and 18c): Under highly uniform conditions, five initial failure zones develop around the borehole. With further loading, these zones interconnect via tensile and shear cracks, creating symmetrical V-shaped failure zones. Compared to $m = 3.5$ (Figs. 17b and 18b), the failure areas have clearly defined boundaries and denser crack distributions.
(3) Under $K = 0.5$ (Figs. 17d–f and 19): Symmetrical V-shaped failure zones form in all three samples, oriented along the direction of minimum horizontal principal stress. As the homogeneity coefficient increases, the extent of these failure zones decreases, with cracks becoming more localized. The crack density at breakout decreases from 9.1 % to 2.5 %, particularly for shear cracks.

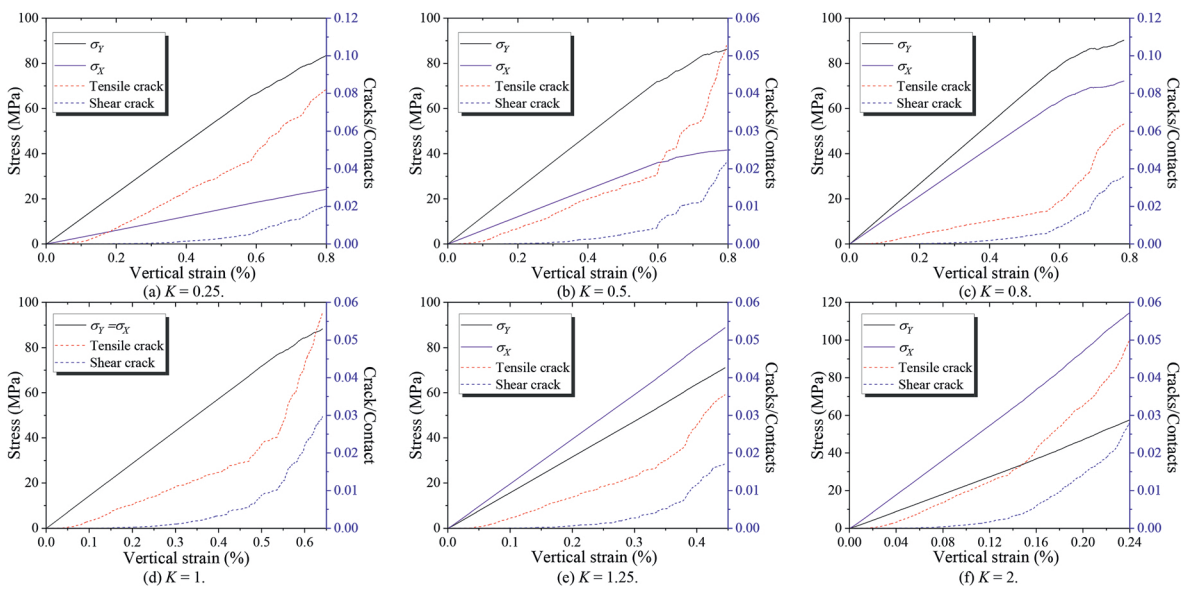

Fig. 15. Evolution of stress-strain relationship and crack density under hydrostatic loading.

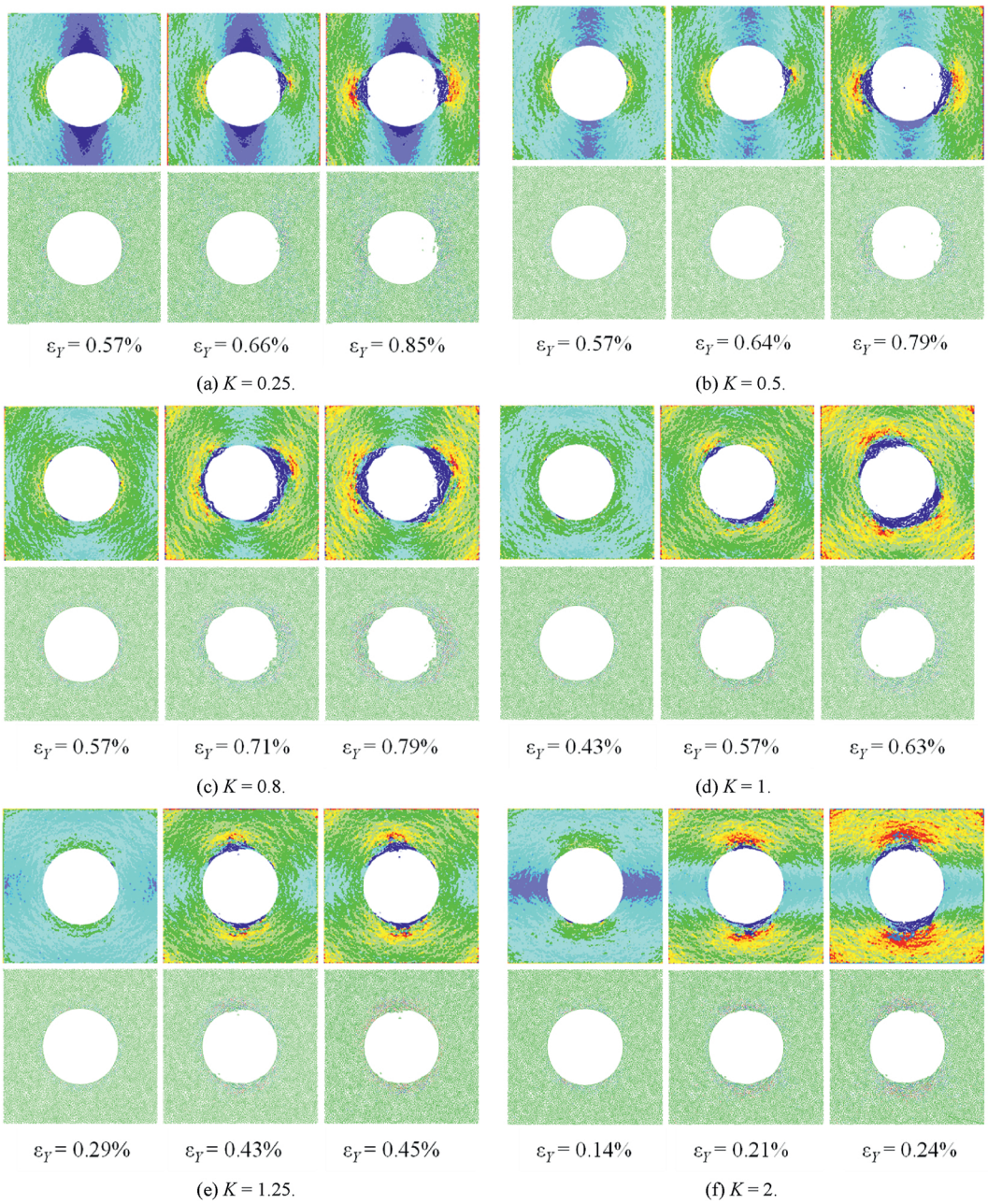

Fig. 16. The maximum principal stress and crack distribution (tensile cracks are blue and shear cracks are red) of the borehole breakout under different lateral stresses coefficients.

Thus, heterogeneity influences both the processes of crack initiation and damage zone evolution during borehole breakout and the corresponding macroscopic failure patterns.

4.5. Influence of borehole diameter on borehole breakout

Under the hydrostatic loading (K = 1), borehole size effects were studied by elevating the diameter from 2 mm to 20 mm. Fig. 20a shows that the critical hydrostatic pressure required for breakout decreases as the borehole enlarges. Because these values come from a 2D model—lacking the out-of-plane confinement present in triaxial laboratory tests—they are lower than corresponding experimental measurements. As the diameter increases, the failure mode shifts, namely tensile cracks become dominant, shear cracks diminish, and the tensile-to-shear crack ratio drops from 5.47 to 1.01. At this critical pressure, the maximum principal stress is tangential ($\sigma_{\theta\theta}$), while the minimum principal stress is radial (σ_{rr}) (Haimson, 2007; Duan and Kwok, 2016):

$$\sigma_{\theta\theta} = P^* \frac{b^2}{b^2 - a^2}\left(1 + \frac{a^2}{r^2}\right) \tag{4}$$

$$\sigma_{rr} = P^* \frac{b^2}{b^2 - a^2}\left(1 - \frac{a^2}{r^2}\right) \tag{5}$$

where b represents half the sample width (b = 25 mm).

Fig. 20b shows the relationship between the uniaxial compressive strength (UCS)-normalized critical tangential stress

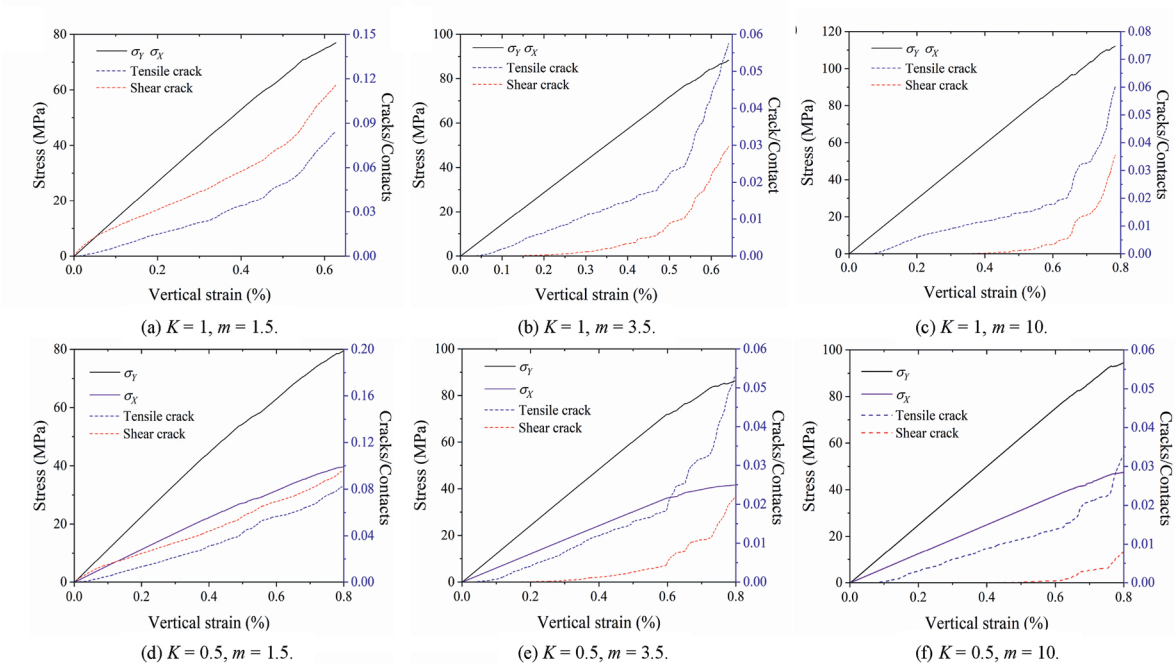

Fig. 17. Stress-strain curve and the crack growth trends under different homogeneity index when $K = 1$ and 0.5.

and borehole diameter, exhibiting a general decline as borehole diameter grows. This size effect, observed across various rock types in both experimental and numerical studies (Dresen et al., 2010; Meier et al., 2013), occurs despite the fact that theoretical stress concentration factors at the borehole wall in purely elastic media are diameter-independent (Houska, 1981). This phenomenon can be explained by considering stress distribution patterns. Larger boreholes create more gradual stress gradients away from the wall, exposing greater volumes of rock to near-peak stress conditions (Zoback et al., 1985). In heterogeneous rocks containing natural discontinuities such as microcracks and grain boundaries (Zweben and Rosen, 1970), the increased volume of highly stressed material around larger boreholes enhances the likelihood of critical flaws experiencing failure-inducing stresses, thereby reducing overall borehole strength.

4.6. Discussion

Our heterogeneous UDEC Voronoi modeling approach offers significant practical utility for analyzing borehole breakouts in various rock formations. By incorporating Weibull-distributed contact parameters, we move beyond traditional homogeneous assumptions to capture near-realistic stress concentrations and crack propagation mechanisms that govern macroscopic failure patterns observed in laboratory and field conditions. This validated numerical model complements laboratory testing by enabling systematic exploration of scenarios difficult to physically replicate, such as varying far-field stress states, borehole diameters, and heterogeneity levels. Engineers can predict critical breakout pressures and anticipate failure geometries under site-specific conditions, supporting stability assessments for boreholes, tunnels, and shafts in geo-energy and civil construction projects. Furthermore, by visualizing stress evolution and differentiating between tensile and shear crack development, the model provides mechanistic insights beyond empirical correlations, informing drilling parameters, mud pressure requirements, and support design strategies. While our 2D approach cannot fully capture 3D stress effects on the borehole deformation, it effectively reproduces fundamental V-shaped breakout mechanisms under plane-strain conditions, advancing borehole stability analysis in complex geological environments.

Several key research directions could build upon this work. The current study emphasized the role of inter-grain heterogeneity in the macroscopic mechanical response of the simulated sandstone of an unvaried microstructure (grain geometry, distribution, and topology). Several studies have highlighted the importance of grain structure in accurate mimicking of brittle deformation of rocks (Li et al., 2017; Zhao et al., 2021). How the microstructure affects the borehole breakout in sandstone will be quantified by the mature technique of grain structure replication in DEM (Chen and Konietzky, 2014; Li et al., 2018). 3D modeling would capture intermediate principal stress effects and the complex, non-symmetrical breakout patterns observed in field environments (Haghgouei et al., 2025; Zhang et al., 2025). Additionally, incorporating thermo-hydro-mechanical coupling would extend the model's applicability to geo-energy applications where temperature gradients and fluid pressure interactions significantly affect borehole stability.

5. Conclusions

In this study, we first examined the physicomechanical properties of red sandstone through laboratory tests and prepared hollow and thick-walled cylindrical samples with borehole diameters of 10 mm, 15 mm, and 20 mm for performing borehole breakout tests under the hydrostatic pressure condition. Using the UDEC, we established a heterogeneous rock model by assuming that contact mechanical properties follow a Weibull distribution. The effects of rock heterogeneity, far-field stress, and borehole diameter on borehole breakout were systematically explored. The key findings are as follows:

(1) From the laboratory perspective, under a hydrostatic pressure, the borehole breakout begins at the axial center of the

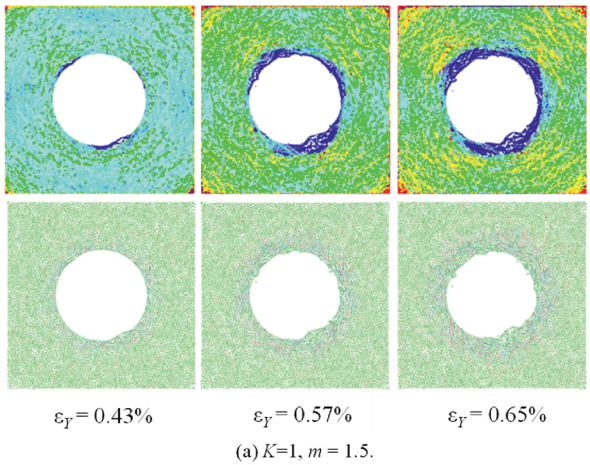

Fig. 18. The maximum principal stress and crack distribution of the borehole breakout with different homogeneity coefficients when K = 1. The tensile crack is in blue and shear crack is in red.

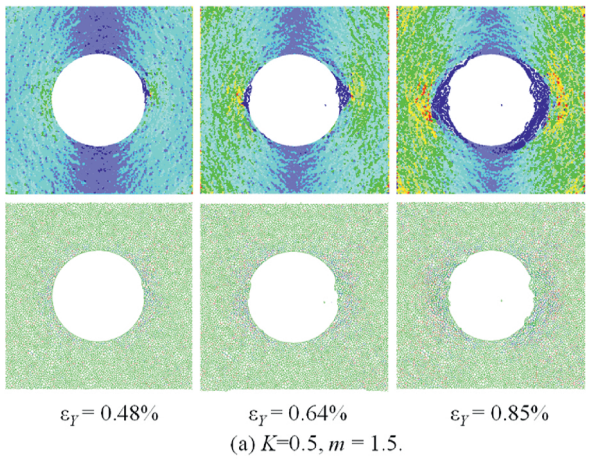

Fig. 19. The maximum principal stress and crack distribution of the borehole breakout with different homogeneity coefficients when K = 0.5. The tensile crack is blue and shear crack is in red.

sample and advances toward both ends, causing the borehole to evolve into a spindle shape. Tensile cracks dominate the failure process due to heterogeneity, and cracks tend to cluster in two opposing zones around the hole, where rock sheets initially form and then peel off to develop symmetrical V-shaped damage regions. In the later stages of loading, caving occurs on the borehole wall in the direction perpendicular to these V-shaped zones. Additional sidewall spalling caused by cracks parallel to the main failure region leads to elliptical features in the failure zone.

(2) By introducing heterogeneity through Weibull-distributed contact parameters, the UDEC model reproduces rock failure under uniaxial and conventional triaxial compression. The progression from initial crack formation to final

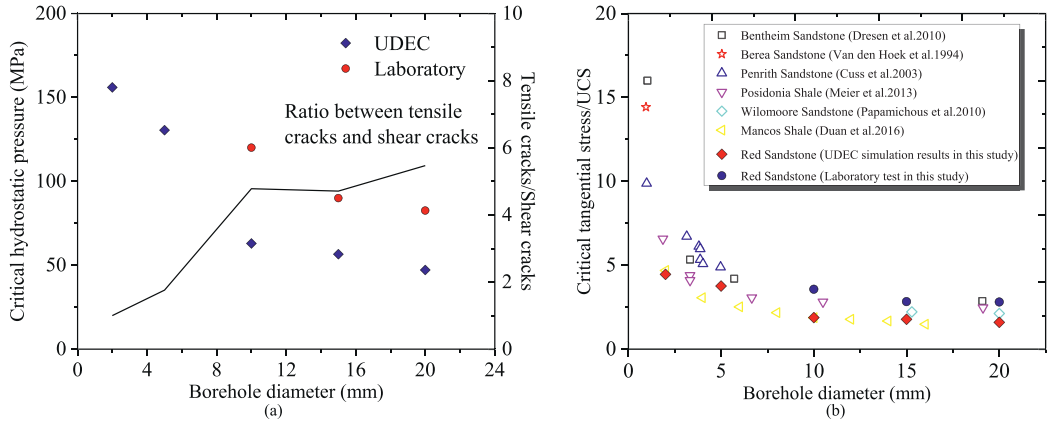

Fig. 20. Effect of borehole diameter on: (a) critical hydrostatic pressure for borehole breakout nucleation and the ratio of tensile to shear cracks; and (b) UCS-normalized critical tangential stress at the borehole wall.

coalescence closely matches experimental observations, confirming the model's validity. This heterogeneous UDEC model also captures the stress-induced borehole breakout process under hydrostatic conditions, reproducing the combined tensile–shear cracking, thin rock slice formation, and gradual exfoliation observed in laboratory tests.

(3) When the lateral pressure coefficient $K = 1.0$, V-shaped failure zones appear in the region of compressive stress concentration and align with the minimum horizontal stress direction. As borehole diameter decreases, the critical hydrostatic pressure required for breakout increases, and the proportion of tensile cracks decreases relative to shear cracks. Rock heterogeneity further influences the breakout path and final geometry.

(4) Our findings on how the stress regime and borehole geometry affect borehole instability in heterogenous rocks facilitate safer design and operations and more accurate examination of in-situ stress in geo-energy engineering. The current work emphasizes the borehole deformation under hydrostatic states and future study will center on 3D modeling under complex stress conditions that are more representative of field geo-mechanical settings.

CRediT authorship contribution statement

Yingchun Li: Writing – review & editing, Writing – original draft, Resources, Methodology, Formal analysis, Conceptualization. **Jiazhi Zhang:** Writing – original draft, Methodology, Formal analysis, Data curation. **Changyi Zuo:** Conceptualization, Formal analysis, Methodology, Supervision, Writing – review & editing. **Kang Duan:** Writing – review & editing, Resources, Methodology, Formal analysis.

Declaration of competing interest

The authors declare that they have no known competing financial interests or personal relationships that could have appeared to influence the work reported in this paper.

Acknowledgements

We thank the financial support from the National Natural Science Foundation of China (Grant No. 42472336). We also thank the anonymous reviewers for their constructive comments and suggestions that substantially improved the manuscript quality.

References

Addis, M.A., Barton, N.R., Bandis, S.C., Henry, J.P., 1990. Laboratory Studies on the Stability of Vertical and Deviated Boreholes. SPE Annu. Tech. Conf. Exhib. SPE.
Bell, J.S., Gough, D.I., 1979. Northeast-southwest compressive stress in Alberta evidence from oil wells. Earth Planet Sci. Lett. 2, 475–482.
Brudy, M., Zoback, M.D., 1999. Drilling-induced tensile wall-fractures: implications for determination of in-situ stress orientation and magnitude. Int. J. Rock Mech. Min. Sci. 2, 191–215.
Cerasi, P., Papamichos, E., Stenebråten, J.F., 2005. Quantitative sand-production prediction: friction-dominated flow model. In: The SPE Latin American and Caribbean Petroleum Engineering Conference. SPE.
Chen, W., Konietzky, H., 2014. Simulation of heterogeneity, creep, damage and lifetime for loaded brittle rocks. Tectonophysics 1, 164–175.
Cuss, R.J., Rutter, E.H., Holloway, R.F., 2003. Experimental observations of the mechanics of borehole failure in porous sandstone. Int. J. Rock Mech. Min. Sci. 5, 747–761.
Ding, X., Zhang, L., Zhu, H., Zhang, Q., 2014. Effect of model scale and particle size distribution on PFC3D simulation results. Rock Mech. Rock Eng. 6, 2139–2156.
Dresen, G., Stanchits, S., Rybacki, E., 2010. Borehole breakout evolution through acoustic emission location analysis. Int. J. Rock Mech. Min. Sci. 3, 426–435.
Duan, K., Kwok, C.Y., 2016. Evolution of stress-induced borehole breakout in inherently anisotropic rock: insights from discrete element modeling. J. Geophys. Res. Solid Earth 4, 2361–2381.
Ewy, R.T., Cook, N.G.W., 1990. Deformation and fracture around cylindrical openings in rock-I. Observations and analysis of deformations. Int. J. Rock Mech. Min. Sci. 5, 387–407.
Fakhimi, A., Carvalho, F., Ishida, T., Labuz, J.F., 2002. Simulation of failure around a circular opening in rock. Int. J. Rock Mech. Min. Sci. 4, 507–515.
Gao, F.Q., Stead, D., 2014. The application of a modified Voronoi logic to brittle fracture modelling at the laboratory and field scale. Int. J. Rock Mech. Min. Sci. 1–14.
Gao, F., Stead, D., Elmo, D., 2016. Numerical simulation of microstructure of brittle rock using a grain-breakable distinct element grain-based model. Comput. Geotech. 203–217.
Ghazvinian, E., Diederichs, M.S., Quey, R., 2014. 3D random voronoi grain-based models for simulation of brittle rock damage and fabric-guided micro-fracturing. J. Rock Mech. Geotech. Eng. 6, 506–521.
Gough, D.I., Bell, J.S., 1981. Stress orientations from oil-well fractures in Alberta and Texas. Can. J. Earth Sci. 3, 638–645.
Haghgouei, H., Nermoen, A., Lavrov, A., 2025. Numerical investigation of wellbore damage due to drill string lateral vibration. J. Rock Mech. Geotech. Eng. 3, 1287–1301.
Haimson, B., 2007. Micromechanisms of borehole instability leading to breakouts in rocks. Int. J. Rock Mech. Min. Sci. 2, 157–173.
Haimson, B., Kovacich, J., 2003. Borehole instability in high-porosity Berea sandstone and factors affecting dimensions and shape of fracture-like breakouts. Eng. Geol. 3–4, 219–231.
Haimson, B., Lee, H., 2004. Borehole breakouts and compaction bands in two high-porosity sandstones. Int. J. Rock Mech. Min. Sci. 2, 287–301.
Haimson, B., Song, I., 1993. Laboratory study of borehole breakouts in cordova cream: a case of shear failure mechanism. Int. J. Rock Mech. Min. Sci. 7, 1047–1056.
Hajiabdolmajid, V., Kaiser, P.K., Martin, C.D., 2002. Modelling brittle failure of rock.

Int. J. Rock Mech. Min. Sci. 6, 731–741.
Herrick, C.G., Haimson, B.C., 1994. Modeling of episodic failure leading to borehole breakouts in Alabama limestone. 1st North Am. Rock Mech. Symp. NARMS 1994, pp. 217–224.
Houska, J., 1981. Fundamentals of rock mechanics. Eng. Geol. 4, 284–285.
Itasca, 2019. UDEC — Universal Distinct Element Code. Itasca Consulting Group.
Justo, J., Konietzky, H., Castro, J., 2022. Voronoi-based discrete element analyses to assess the influence of the grain size and its uniformity on the apparent fracture toughness of notched rock specimens. Rock Mech. Rock Eng. 5, 2861–2877.
Kazerani, T., Zhao, J., 2010. Micromechanical parameters in bonded particle method for modelling of brittle material failure. Int. J. Numer. Anal. Methods GeoMech. 18, 1877–1895.
Lan, H., Martin, C.D., Hu, B., 2010. Effect of heterogeneity of brittle rock on micromechanical extensile behavior during compression loading. J. Geophys. Res. Solid Earth B1.
Lan, H., Martin, C.D., Andersson, J.C., 2013. Evolution of in situ rock mass damage induced by mechanical-thermal loading. Rock Mech. Rock Eng. 1.
Lee, H., Moon, T., Haimson, B.C., 2016. Borehole breakouts induced in Arkosic sandstones and a discrete element analysis. Rock Mech. Rock Eng. 4, 1369–1388.
Leeman, E.R., 1999. The measurement of stress in rock part 1 the principles of rock stress measurements. J. South African Inst. Min. Metall. 1, 19–25.
Li, J., Konietzky, H., Frühwirt, T., 2017. Voronoi-based DEM simulation approach for sandstone considering grain structure and pore size. Rock Mech. Rock Eng. 10, 2749–2761.
Li, X.F., Zhang, Q.B., Li, H.B., Zhao, J., 2018. Grain-based discrete element method (GB-DEM) modelling of multi-scale fracturing in rocks under dynamic loading. Rock Mech. Rock Eng. 12, 3785–3817.
Li, Y., Qu, Y., He, Q., Tang, C., 2020. Mesoscale numerical study on the evolution of borehole breakout in heterogeneous rocks. Int. J. Numer. Anal. Methods GeoMech. 8, 1219–1236.
Lin, H., Oh, J., Canbulat, I., Stacey, T.R., 2020a. Experimental and analytical investigations of the effect of hole size on borehole breakout geometries for estimation of in situ stresses. Rock Mech. Rock Eng. 2, 781–798.
Lin, H., Oh, J., Canbulat, I., Stacey, T.R., 2020b. Experimental and analytical investigations of the effect of hole size on borehole breakout geometries for estimation of in situ stresses. Rock Mech. Rock Eng. 2, 781–798.
Meier, T., Rybacki, E., Reinicke, A., Dresen, G., 2013. Influence of borehole diameter on the formation of borehole breakouts in black shale. Int. J. Rock Mech. Min. Sci. 74–85.
Oh, J., Li, Y., Mitra, R., Canbulat, I., 2017. A numerical study on dilation of a Saw-toothed rock joint under direct shear. Rock Mech. Rock Eng. 4, 913–925.
Papamichos, E., 2010. Borehole failure analysis in a sandstone under anisotropic stresses. Int. J. Numer. Anal. Methods GeoMech. 6, 581–603.
Plumb, R.A., Hickman, S.H., 1985. Stress-induced borehole elongation: a comparison between the four-arm dipmeter and the borehole televiewer in the auburn geothermal well. J. Geophys. Res. B7, 5513–5521.
Tang, C.A., Yang, W.T., Fu, Y.F., Xu, X.H., 1998. A new approach to numerical method of modelling geological processes and rock engineering problems - continuum to discontinuum and linearity to nonlinearity. Eng. Geol. 3–4, 207–214.
Tang, C.A., Liu, H., Lee, P.K.K., Tsui, Y., Tham, L.G., 2000. Numerical studies of the influence of microstructure on rock failure in uniaxial compression - part I: effect of heterogeneity. Int. J. Rock Mech. Min. Sci. 4, 555–569.
Van Den Hoek, P.J., 2001. Prediction of different types of cavity failure using bifurcation theory. DC Rocks 2001 - 38th U.S. Symp. Rock Mech 45–52.
Wang, Y., Yang, H., Song, K., Chen, C., Li, H., Li, X., 2024. The energy characteristics of columnar jointed basalt size effect considering the occurrence sequence and magnitude of micro-cracks. Rock Mech. Rock Eng. 12, 11139–11175.
Xiang, Z., Moon, T., Si, G., Oh, J., Canbulat, I., 2023. Numerical analysis of V-shaped borehole breakout using three-dimensional discrete-element method. Rock Mech. Rock Eng. 4, 3197–3214.
Yazdani, M., Fatehi, Marji M., Soltanian, H., Najafi, M., Sanei, M., 2024. Discrete elements analysis of sand production mechanism in oil well considering effects of in-situ stress and fluid pressure. J. Min. Environ. 4, 1509–1525.
Yousefian, H., Marji, M.F., Soltanian, H., Abaollahipour, A., Pourmazahri, Y., 2020. Wellbore trajectory optimization of an Iranian oilfield based on mud pressure and failure zone. J. Min. Environ. 1, 193–220.
Yu, J., Wang, T., Liu, K., Wang, Y., Tang, C., Zhu, B., 2025. Mechanical and failure behaviors of columnar jointed basalts (CJBs): 3D microscopic reconstruction and modeling. Eng. Fract. Mech., 110778
Zhang, J., 2013. Borehole stability analysis accounting for anisotropies in drilling to weak bedding planes. Int. J. Rock Mech. Min. Sci. 160–170.
Zhang, S., Jiang, L., Shen, H., Qin, X., Zhao, X., 2025. Quantifying the progressive development of breakouts initiated from pre-existing fractures: implications for local stress heterogeneity. Int. J. Rock Mech. Min. Sci., 106078
Zhao, X., Elsworth, D., He, Y., Hu, W., Wang, T., 2021. A grain texture model to investigate effects of grain shape and orientation on macro-mechanical behavior of crystalline rock. Int. J. Rock Mech. Min. 148, 104971.
Zheng, Z., Kemeny, J., Cook, N.G.W., 1989. Analysis of borehole breakouts. J. Geophys. Res. Solid Earth B6, 7171–7182.
Zhu, W.C., Bruhns, O.T., 2008. Simulating excavation damaged zone around a circular opening under hydromechanical conditions. Int. J. Rock Mech. Min. Sci. 5, 815–830.
Zhu, W.C., Liu, J., Tang, C.A., Zhao, X.D., Brady, B.H., 2005. Simulation of progressive fracturing processes around underground excavations under biaxial compression. Tunn. Undergr. Space Technol. 3, 231–247.
Zoback, M.D., Moos, D., Mastin, L., Anderson, R.N., 1985. Well bore breakouts and in situ stress. J. Geophys. Res. B7, 5523–5530.
Zweben, C., Rosen, B.W., 1970. A statistical theory of material strength with application to composite materials. J. Mech. Phys. Solid. 3, 189–206.

Dr. Yingchun Li joined Department of Civil Engineering, School of Infrastructure Engineering, Dalian University of Technology, China in 2017. Dr. Li obtained BE in engineering from School of Mines, China University of Mining and Technology (CUMT), and his PhD from School of Mining Engineering, University of New South Wales, Sydney, Australia in 2016. His research interests focus on fundamentals and applications of rock mechanics in deep underground space and geo-resources engineering. He received several grants from the National Natural Science Foundation of China and the Ministry of Science and Technology, China. He has published more than 90 scientific papers.